

Complex dielectric behaviours in $BiFeO_3/Bi_2Fe_4O_9$ ceramics

Gilad Orr^a, Andrey Gorychev^a, Paul Ben Ishai^{a,*}

^a*Department of Physics, Ariel University, Ariel 40700, Israel*

Abstract

The complex dielectric permittivity of a sintered ceramic tablet consisting of 70.5 % $BiFeO_3$ and 27.7% $Bi_2Fe_4O_9$ was analyzed as a function of temperature from -120 °C to 230 °C. The results reveal a complicated dielectric response with temperature activated relaxation features. They also reveal a ferroelectric phase transition that decayed with repeated heating cycles of the tablet. The source of the behaviour is assigned to relaxation processes happening along the grain boundaries of differing compositions in the tablet. The origin of the phase transition is traced to locally induced strains on grain boundaries because of unit cell size mismatch between $BiFeO_3$ and $Bi_2Fe_4O_9$.

Keywords: Dielectric response, $BiFeO_3$, $Bi_2Fe_4O_9$, Multiferroics, complex permittivity

1. Introduction

Bismuth Ferrites are the poster boys for multi-ferroics, a class of materials capable of simultaneously hosting both ferromagnetic and ferroelectric properties and first predicted by P. Curie [1]. Of these Bismuth Ferrite, $BiFeO_3$, first studied seriously by Smolensky in 1958 and later produced as a single phase [2], has taken the podium position as the archetypal multi-ferroic [3], [4]. The unit cell of Bismuth Ferrite is a perovskite type structure at room temperature belonging to the space group $R3c$ [5], [6] with 2 formula units involved in the basic unit cell [7], reproduced in Figure 1, resulting in a rhombohedral.

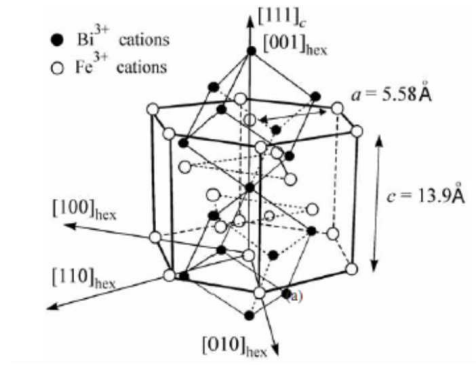


Figure 1: The unit cell of $BiFeO_3$ (reproduced from Ref. [7]) the axis directions are given for both the cubic and hexagonal frames of reference. For clarity the oxygen ions are not shown.

For clarity the oxygen atoms are not shown. They occupy the face centers of the Bismuth cubes. As has been noted this structure results in a room temperature ferroelectric polarization along the

*Corresponding author paulbi@ariel.ac.il

Email addresses: gilad.orr@ariel.ac.il (Gilad Orr), paulbi@ariel.ac.il (Paul Ben Ishai)

[111]cubic axis as well as a distortion to the oxygen octahedra by rotating it approximately 11-14° around the [111] axis [4]. This leads to an Fe-O-Fe angle of $\theta = 154\text{--}156^\circ$ [4], the significance of which is to control both the magnetic ordering and orbital overlap between Fe and O. This is the source of BFO's magnetic behavior. The ferroelectric transition [4] is at $T=825^\circ\text{C}$, meaning that the pure BFO is ferroelectric and anti-ferromagnetic (type G) at room temperature [6], [8]. Unlike most inorganic perovskites the polarization axis is along the diagonal [111] perovskite direction [9], while its magnetic axis is perpendicular to the same axis. Indeed, its intrinsic polarization along this axis has been measured at $100\ \mu\text{C}/\text{cm}^2$. The Neel temperature for BFO is around 640 K (367°C) and above this the structure tends towards tetragonal [6]. Beyond the ferroelectric transition the structure resolves as cubic. Currently BFO and its derivatives are some of the rare room temperature multi-ferroics and as such have found many applications in nanoelectronic devices [10], spintronic applications [11], photovoltaics and others [12]. However, single crystals are not simple to grow and frequently it is more feasible to work with thin films or ceramics [8]. Because of the volatility of Bi^{3+} and the aggregation of oxygen vacancies along poly crystalline boundaries, it is not uncommon during sintering for the formation of secondary phases, such as the mullite-like structured $\text{Bi}_2\text{Fe}_4\text{O}_9$ [13]. $\text{Bi}_2\text{Fe}_4\text{O}_9$ is an intriguing multiferroic in its own right. Unlike BFO is paramagnetic at room temperature and its structure is very different, belonging to the orthorhombic $Pbam$ space group [13]. Unlike BFO, Bi^{2+} ions sit in the channels formed by the FeO_6 octahedra, parallel to the c-axis. The result is that the stereochemically $6s^2$ Lone Pair Electrons (LEP), responsible for its rather poor ferroelectric behaviour [14], are similarly aligned [15]. Its Néel temperature is 264 K and at room temperature it is antiferromagnetic. A comparison of unit cell sizes of the two reveals that there is considerable mismatch between them (see figure 2). Furthermore, the net dipole moment from the LEP is aligned along the c axis for the mullite-type structure, rather than along the diagonal as for the perovskite structure of BFO. One must assume that in mixed ceramics the domain boundary between the two phases will be a source of rich dielectric behaviors.

The dielectric permittivity of polycrystalline [14] BFO/BFO derivatives and ceramics [16] and has been studied in the past with an emphasis on the high dielectric permittivities that can be obtained with such materials .

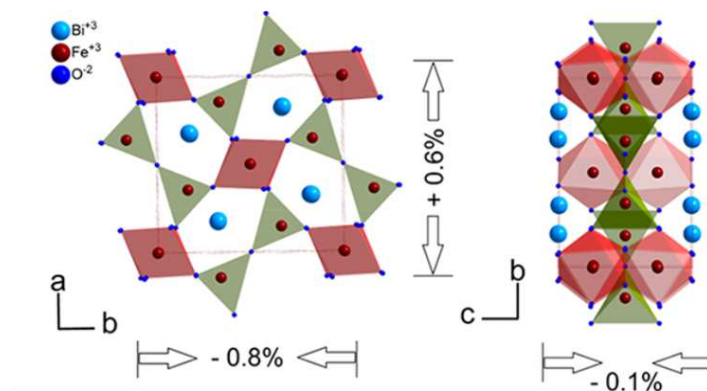


Figure 2: A comparison of the unit cell sizes between BFO and mullite-type $\text{Bi}_2\text{Fe}_4\text{O}_9$. reproduced from [13]

In the case of Markiewicz et al. [16] the secondary phase was $\text{Bi}_{25}\text{FeO}_{40}$ and they noticed a rich dielectric landscape. Most of the behaviour could be related to motion along grain boundaries, along with distinct dielectric processes arising from carrier hopping between Fe^{2+} and Fe^{3+} sites, as was shown by X-ray Photoelectron spectroscopy or the short range hopping of oxygen vacancies.

In this study we concentrate on $BFO/Bi_2Fe_4O_9$ ceramics and consider the characteristics of the observed behaviours in terms of the frequency and temperature trends, rather than in terms of their dielectric constants, as is traditionally done [14], [17].

2. Materials Preparation

BFO synthesis results in a composition of three stable phases, depending on the ratio between the Fe and Bi based molecules in the starting materials, the synthesis temperature, the annealing history and impurities [18]. The three stable phases are $BiFeO_4$, the mullite-like $Bi_2Fe_4O_9$ and sillenite-like $Bi_{25}FeO_{40}$. In this work we are interested in the BFO and mullite-like phases which are non-symmetric while avoiding the cubic $Bi_{25}FeO_{40}$. In order to compare similar previous work in the field [16] we opted for a low temperature sol-gel based synthesis [19] that maintains the grain size in the tenths of nanometers.

$Bi(NO_3)_3 \cdot 5H_2O$ and $Fe(NO_3)_3 \cdot 9H_2O$ were dissolved in distilled water forming a 0.015 mole solution of each. This was followed by mixing both solutions and adding 0.3 cc of 70% nitric acid (HNO_3). The solution was stirred for half an hour after which a 0.05 mole solution of tartaric acid was added followed by another half an hour of stirring. The material was poured into a specially assembled temperature controlled flask with a stirring mechanism where the temperature was maintained at 100 °C for approximately 7 hours. The resulting gel was dried at 100 °C until it became an orange brown powder. Disks with 12.7 mm diameter were from 600 mg of powder using a pressure of approximately 100MPa and then annealed at 650 °C for 2 hours. The annealing temperature was chosen, based on Selbach's work [18], [20] which has demonstrated that, based on Gibbs energy, within the 447~767 °C temperature range, $BiFeO_3$ is a metastable compound with $Bi_2Fe_4O_9$ and $Bi_{25}FeO_{40}$ being slightly more stable. Hence the material, slowly transforms into those compounds. Due to the 1:1 ratio between the Bi and Fe the mullite-like structure was expected to prevail.

3. Methodology

3.1. XRD

XRD phase structure acquisition of the synthesized material disks prior to sintering and after, was carried out using a PANalytical X'Pert Pro fitted with a Cu $K\alpha$ source ($\lambda=1.5406\text{\AA}$). Phase analysis was based on Rietveld refinement routines (FullProf Suite) [21] with the peaks compared to those generated using the Crystallography Open Database (COD) [22]. Particle size was estimated using parameters obtained by fitting of the peaks in Matlab using the Scherrer equation[23].

3.2. Dielectric Measurements

Silver electrodes of 4 mm diameter were deposited by vapour deposition on the ceramic tablet of 0.48 mm thickness. Dielectric measurements were made use a Novocontrol Broadband Dielectric Spectrometer based on an Alpha Impedance Analyser [24] in the frequency range 0.2 Hz to 105 Hz. Temperature control was provided a Quattro PID temperature controller (Novocontrol GmbH, Hamburg, Germany). The initial temperature protocol was 20°C to -120°C and then -120°C to 200°C. A further measurement was made at 90°C under a bias voltage 0 V to -40 V, -40 V to 40 V and 40 V to 0 V with a 4 V voltage step . The sample was cooled and stored at room temperature for a month and the measurement repeated in the same frequency range, but temperature range from 0°C to 230°C.

4. Results and Discussion

4.1. XRD

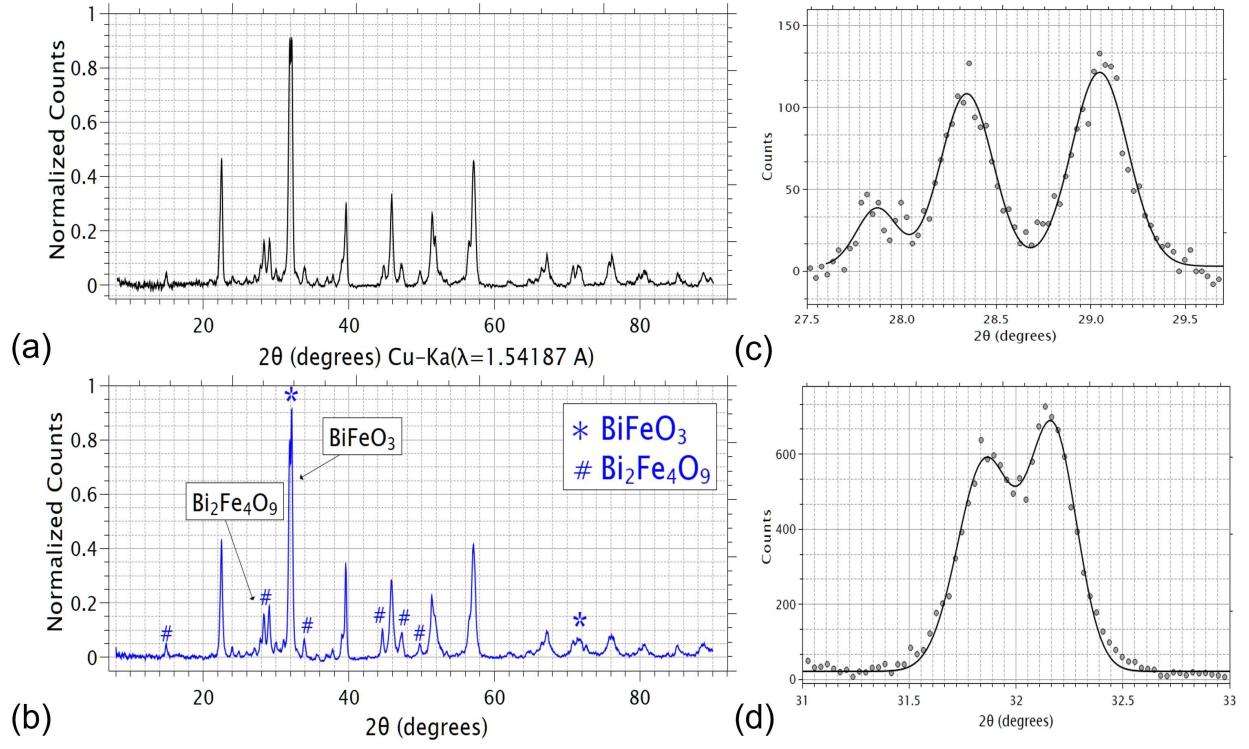


Figure 3: XRD patterns for a *BFO* tablet. (a) powder, (b) sintered tablet. The characteristic peaks for *BFO* and $\text{Bi}_2\text{Fe}_4\text{O}_9$ are labelled, (c) a gaussian fit for the $\text{Bi}_2\text{Fe}_4\text{O}_9$ feature and (d) gaussian fit for the *BFO* feature.

The XRD patterns for the powder and the sintered tablet are presented in figure 3. A direct comparison of the patterns in figure (a) and (b) reveals little change indicating the sintering did not change composition. From Rietveld refinement [23] the composition of the tablet is 70.5 % *BFO*, 27.7% $\text{Bi}_2\text{Fe}_4\text{O}_9$ and 1.8 % $\text{Bi}_{25}\text{FeO}_{40}$. To assess particle size, the dominant features of the two main constituents were fitted using gaussians (shown in panels (c) and (d)).

$$f(\theta) = \sqrt{\frac{2}{\pi}} \cdot \frac{A_i}{\sigma_i} \cdot \exp\left(-2 \left(\frac{2\theta - 2\theta_i}{\sigma_i}\right)^2\right) \quad (1)$$

Where A_i is the amplitude, θ_i is the position and σ_i is the width of peak i . The results are listed in table 1. Particle size is derived using the Scherrer equation [25],

$$d = \frac{K \cdot \lambda}{\sigma_i \cdot \cos(\theta_i)} \quad (2)$$

Where K is the Scherrer shape factor, usually taken as 0.92 for cubic grains, and λ is the X-ray wavelength (1.54187 Å). The size range calculated by equation 2 is shown in table 1. *BFO* crystallites are notably larger than the secondary phase $\text{Bi}_2\text{Fe}_4\text{O}_9$.

	A_1	A_2	$2\theta_1$	$2\theta_2$	σ_1	σ_2	Size (nm)
<i>BFO</i>	179.7	180.2	31.8	32.17	0.257	0.225	31.5-36.9
<i>Bi₂Fe₄O₉</i>	36.5	44.2	28.35	29.05	0.276	0.298	27-29.7

Table 1: The gaussian fitting parameters of figure 3(c) and (d)

4.2. Dielectric Permittivity

The dielectric permittivities and losses for the BFO ceramic tablet are presented in Figure 4. The upper graphs show the dielectric permittivity (a) for the initial measurement and for the final measurement (b). The dielectric losses are shown in the bottom graphs respectively.

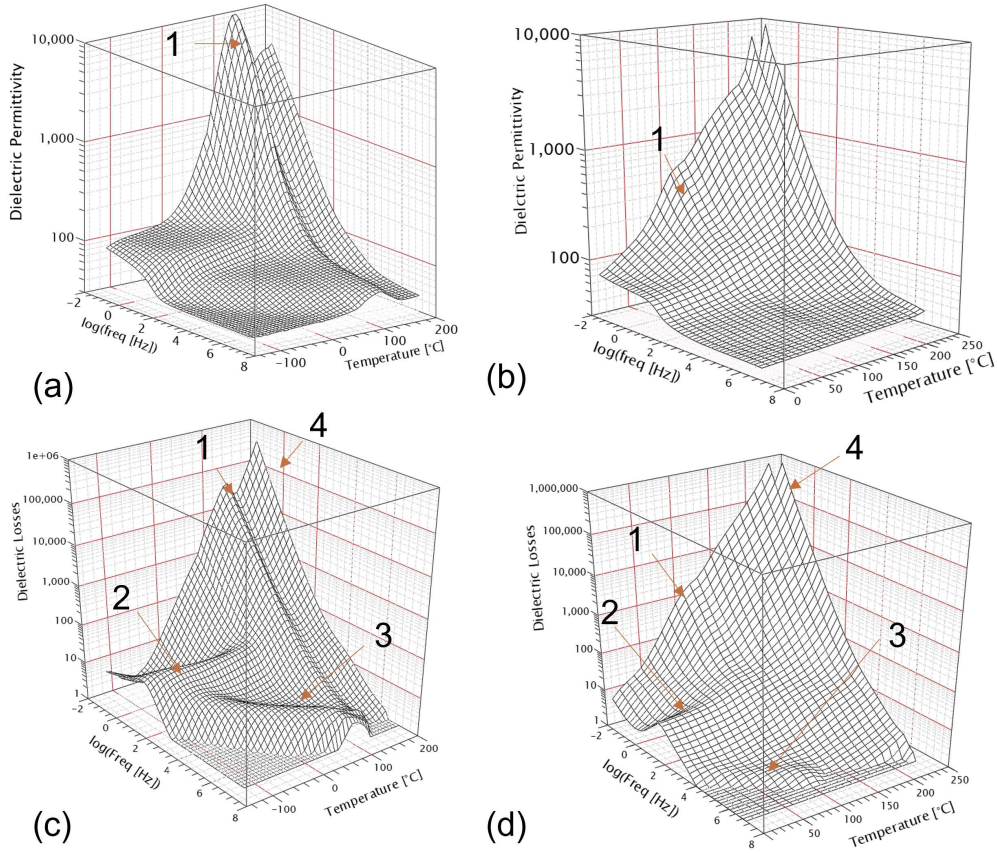


Figure 4: The dielectric permittivity for the first measurement (a) and for the second measurement (b) of the BFO tablet. In the second row are the corresponding dielectric losses, (c) and (d) respectively. The highlighted features of the relaxation landscape are: a second order phase transition (1), an Arrhenius relaxation process with low activation energy (2), a Vogel-Fulcher-Tammenn type relaxation process (3), dc conductivity overlaying low frequency relaxations outside the measurement window (4).

It is apparent that the dielectric landscape is rich, with two relaxations, marked 2 and 3 in the figure, inside the measurement window and dc conductivity is present in the higher temperatures. One notes a phase transition, marked 1 in the figure, with $T_c = 100.6^\circ\text{C}$ (373 K). The transition temperature was established by finding the extremum in the temperature derivative of the dielectric permittivity. While the feature is still present in the second measurement it is greatly diminished, indicating that continued reheating of the tablet has led to a further modification of the phases.

The bias measurement around 90 °C, close to the phase transition temperature of 100.6 °C, revealed no hysteresis. The dielectric permittivity at 0.13309 Hz is presented in Figure 5(a). The vicinity of the phase transition was modelled using the Curie-Weiss expression , $\varepsilon'(T) = C_i/(T - T_c)$, where $i = 1, 2$ for temperatures below and above T_c respectively [26], [27]. According to Landau’s phenomenological theory for phase transitions [26] the ratio, C_1/C_2 , depends on whether the phase transition is first order ($C_1/C_2 = -8$) or second order ($C_1/C_2 = -2$) In our case it is -1.64, close to -2 indicating that this is a second order structural ferroelectric phase transition, consistent with the lack of hysteresis noted in the bias measurement. MacKenzie et al. [14] also noted an anomaly in the dielectric permittivity of $Bi_2Fe_4O_9$ at 252 °C, which they associated with the reported magnetic transition temperature in pure $Bi_2Fe_4O_9$. However, this is far from the anomaly reported here. Another possibility is that it is related to the BFO phase. While the main ferroelectric phase transition is at 825 °C [4], GHz spectroscopy of nearly pure BFO also found phase transition at 130 °C [28]. Catalan et al. suggested that this was due to the presence of secondary phases [4]. Likewise, the mismatch between $BFO/Bi_2Fe_4O_9$ crystallines can lead to large strains, as has been noted in other crystalline systems [29]. Figure 6 of ref [4] shows that a pressure of 4 GPa would be enough to reduce T_c in BFO to 100 °C and this is easily achievable on the local level of the domain boundary [29]. Therefore, we speculate that this transition is a locally induced strain effect on BFO crystallites in the immediate vicinity of $Bi_2Fe_4O_9$ crystallites.

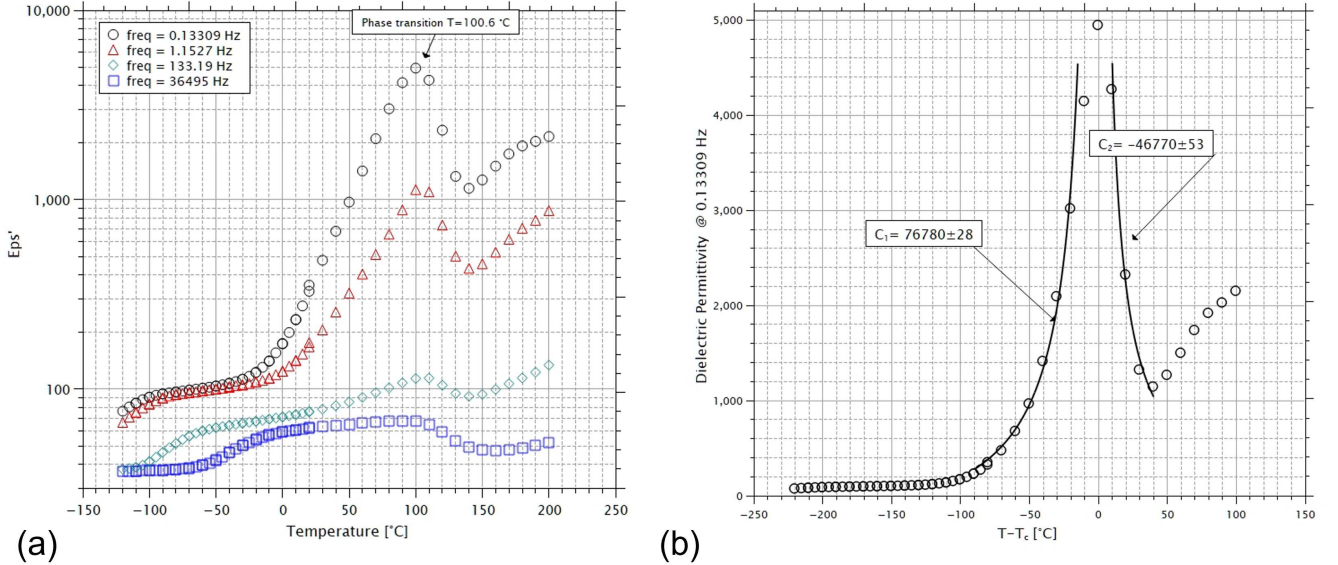


Figure 5: (a) The dielectric permittivity as a function of temperature for 4 frequencies, showing a dominant phase transition at $T_c = 100.6^\circ C$ and (b) Curie-Weiss fitting before and after the phase transition temperature, $\varepsilon'(T) = C_i/(T - T_c)$. The ratio of the constants is $C_1/C_2 = -1.64$, indicating a second order ferroelectric phase transition.

The complex dielectric permittivity, $\varepsilon^*(i\omega) = \varepsilon'(\omega) - i\varepsilon''(\omega)$, where $\varepsilon'(\omega)$ is the dielectric permittivity and $\varepsilon''(\omega)$ is the dielectric losses, was modeled using a sum of 3 Havriliak-Negami (HN) functions along with a dc conductivity term,

$$\varepsilon^*(i\omega) = \varepsilon_\infty + \sum_{j=1}^3 \frac{\Delta\varepsilon_j}{(1 + (i\omega\tau_j)^{\alpha_j})^{\beta_j}} + \frac{\sigma_{dc}}{i\omega\varepsilon_0} \quad (3)$$

Where ε_∞ is the higher frequency contribution to the dielectric permittivity, $\Delta\varepsilon_j$ is the dielectric strength of the j th process, τ_j is the corresponding characteristic relaxation time, $0 < \alpha_j, \beta_j \leq 1$

are the shape parameters, σ_{dc} is the dc conductivity, ω is the cyclic frequency, i is the root of -1 and $\varepsilon_0 = 8.85 \times 10^{-12} \text{ F/m}$ is the permittivity of free space. In the first set of measurements the 3rd process was used to model the tail of relaxations situated at frequencies lower than the bounds of the measurement window but intruding to the data. For the second measurement at high temperatures (above 0 °C) 3 HN processes are found inside the measurement window and so lower frequency processes are modelled using a Left-hand Jonscher function [30], $A \cdot (i\omega)^{-n}$, where A is the amplitude and $0 < n < 1$. The data was modelled using an in house fitting routine, Datama [31], based on Matlab [32]. The software is capable of fitting in the complex plain and exploits a logarithmic measure for the merit function $\chi^2(\varepsilon^*(i\omega_n), \varepsilon^f(i\omega_n, \{x_j\})) = \sum_{n,j} [\log(\varepsilon^*(i\omega_n)) - \log(\varepsilon^f(i\omega_n, \{x_j\}))]^2$, where $\varepsilon^*(i\omega_n)$ is the measurement data at the frequency point ω_n , $\{x_j\}$ is the parameter set defined in equation 3 and $\varepsilon^f(i\omega_n, \{x_j\})$ is the model function value for the parameter set and respective frequency point. The advantage is that for data with values varying by orders of magnitude over the frequency range, equal weight is given in the merit function for all frequency points, leading to a more accurate fit. The dc conductivity for both measurement runs is presented in Figure 7.

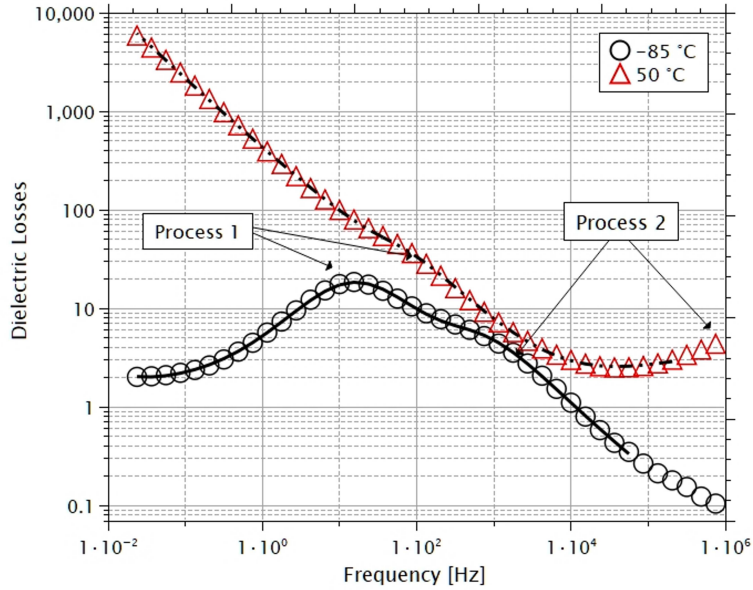


Figure 6: The dielectric losses at -85 °C (circles) and at 50 °C (triangles) for the first measurement run. The solid lines are the fitting function described by equation 3. The 2 dominant processes are labeled

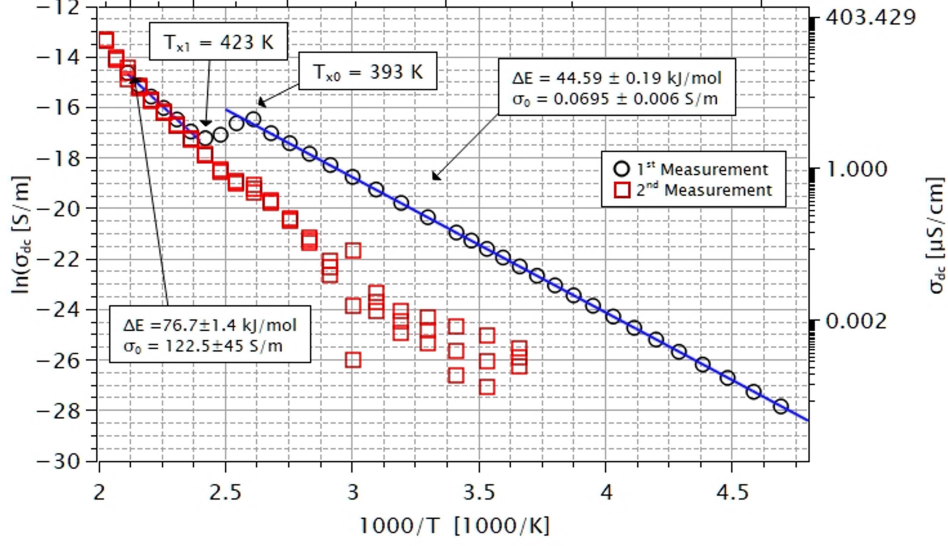


Figure 7: An Arrhenius plot of the dc conductivity for the first (black circles) and second (blue squares) measurement runs. The fitting lines are according to the Arrhenius expression. The sample undergoes a compositional change during the first run between $T=393$ K and $T=423$ K.

In both cases the conductivity is an activated process and obeys the Arrhenius expression for conductivity,

$$\sigma_{dc}(T) = \sigma_0 \exp\left(\frac{-\Delta E}{k_B T}\right) \quad (4)$$

where σ_0 is the high temperature limit of conductivity, T is the temperature in Kelvin, k_B is Boltzmann's coefficient and is the energy of activation for the process. The parameters are listed in Table 2. At $T=393$ K the sample undergoes a compositional change, stabilizing at $T=423$ and resulting in a doubling of the energy of activation. The dc conductivity during the second measurement run matches these new parameters. Usually dc conductivity in perovskite systems. Like *BFO* are assigned to the migration of oxygen vacancies [16], [17]. In mullite-like *Bi₂Fe₄O₉* it has been assigned to intrinsic holes, centered around Oxygen. Reducing *Bi₂Fe₄O₉* by oxygen loss led to an extrinsic n-type semiconductor via $O^{2-} \rightarrow \frac{1}{2}O_2 + 2e^-$ [17]. However, In the case of *BFO* the energies of activation are usually around 0.9 eV to 1.1 eV (87 kJ/mol to 106 kJ/mol), considerably higher than those measured here, although for spark plasma sintering (SPS) of *BFO* a value of $0.67 \pm 0.07 eV$ ($64.6 \pm 6.8 kJ/mol$) was found [33]. In the sillenite like phase *Bi₂₅FeO₄₀* dc conductivity has been measured with an activation energy of $0.52 \pm 0.02 eV$ ($50.2 \pm 1.9 kJ/mol$) [17]. Given the very low percentage of this phase in the sample (1.8 %), it is unlikely that this is the source of conductivity we see. The value of conductivity at 80 °C is $1.8 \times 10^{-7} S/m$ for the first run and $5.8 \times 10^{-10} S/m$ for the second run. For both runs dc conductivity was $4.4 \times 10^{-7} S/m$ at 200 °C. This can be compared to the reported values of $2.77 \times 10^{-7} S/m$ for pure *Bi₂₅FeO₄₀* ceramic [17] at 350 °C and more than $2 \times 10^{-6} S/m$ for *BFO* ceramic [33]. The origin of the low activation energy in SPS *BFO* was attributed to the reduction, caused by the sintering process itself, along grain boundaries. The removal of oxygen from the sample led to an excess of electrons, which in turn led to a reduction of conducting holes by recombination. One can assume that in our sample a similar process had occurred at the grain boundaries between the two dominant compositions. This is further enhanced as a hypothesis by the dramatic change in conductivity

starting a 393 K in the first run. The Novocontrol system maintains the sample temperature by a temperature controlled Nitrogen flow, possibly leading to further oxygen loss in the sample and activation energies close to those reported to SPS BFO.

	Measurement 1 (T<393K)	Measurement 1&2 (T>423K)
$\sigma_0 [S/m]$	0.0695 ± 0.0006	123 ± 45
$\Delta E [kJ/mol]$	44.59 ± 0.19	76.7 ± 1.4

Table 2: The parameters of the Arrhenius fit for dc conductivity.

The fitting reveals two distinct dielectric relaxations in the first measurement and three distinct relaxations in the second, higher temperature measurement. As stated above this indicates that the first temperature run induced further sintering in the sample. The relaxation times for the processes are presented in Figure 8.

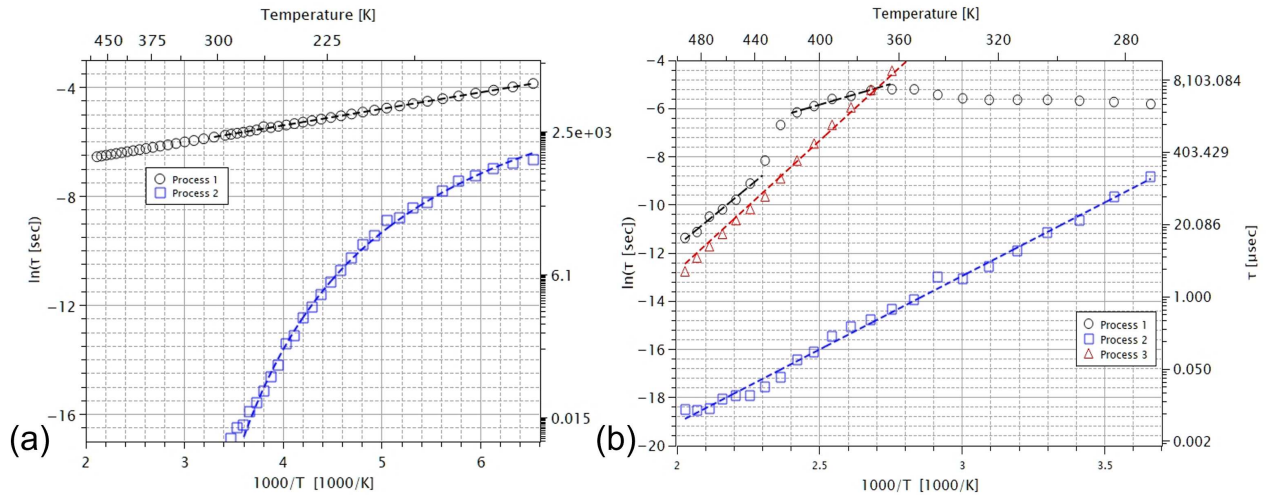


Figure 8: The relaxation times in an Arrhenius plot for the first measurement run (a) and for the second run (b). The first run is dominated by two processes, one weakly temperature activated with an Energy of Activation of $5.04 \pm 0.02 kJ \cdot mol^{-1}$. The second process follows VFT behaviour, indicative of a glassformer. In the second measurement run Process 1 is still present, but greatly modified. Above 360 K (approximately at the indicated Phase transition temperature) it becomes temperature activated, undergoing a further modification at 440 K. Additionally, there is no sign of the glassforming process, but 2 strongly temperature activated processes appear.

The first temperature run, Figure 8(a), is dominated by two processes (aptly marked Process 1 and Process 2 in the figure). Process 1 is Arrhenius with an energy of activation of $\Delta E = 5.04 \pm 0.02 kJ \cdot mol^{-1}$. This range of activation energy is typical of Maxwell- Wagner processes over domain boundaries [34] and we can readily assign it to mismatched grain boundaries in the ceramic. The second process is more puzzling. At first glance it can be modeled by a Vogel Fulcher Tammann (VFT) formula of the form

$$\tau(T) = \tau_0 \exp\left(\frac{E_0}{k(T_0 - T)}\right) \quad (5)$$

With the parameters $\tau_0 = 10^{14} s$, $E_0 = 199 kJ \cdot mol^{-1}$ and $T_0 = 766 K$. The VFT formula is usually associated with a glass transition in dielectric science [35]. However, in this case it can be linked to the dynamic rearrangement of domain boundaries between different crystallites in the

ceramic. Thermodynamically the relaxation time is proportional to the probability of a transition between two energy states to the system,

$$\tau^{-1}(T) \propto P \propto \exp\left(\frac{-\Delta F}{k_B T}\right) \quad (6)$$

Where ΔF is the Helmholtz free energy and k_B is Boltzmann's constant. Formally the Helmholtz energy is given by

$$F = \frac{1}{2}V \sum_{ij} \sigma_{ij} \varepsilon_{ij} - ST + \sum_i \mu_i N_i \quad (7)$$

where, V is the volume, S is the entropy, σ_{ij} and ε_{ij} are the stresses and strains between crystallites i and j respectively, μ_i is the chemical potential of the i species and the N_i is the number density. If the transitions between crystallites of BFO and $Bi_2Fe_4O_9$ are negligible, then the source of the free energy is the mechanic energy caused by the unit cell size mismatch at the grain boundaries (see Figure 2). Thermal energy in this case leads to rearrangements to reduce F to its minimum,

$$\Delta F = \frac{1}{2} \left(\Delta V \sum_{ij} \sigma_{ij} \varepsilon_{ij} + V \sum_{ij} \Delta(\sigma_{ij} \varepsilon_{ij}) \right) - T \Delta S + \sum_i \Delta(\mu_i N_i) \quad (8)$$

If the boundary strains are proportional to the unit cell sizes and these do not vary, then the variation in free energy depends solely on the changes in volume as the crystallites coalesce (the assumption that there are negligible transition means that the last term in equation 8 can be ignored). The volume ΔV is understood to refer to any mesoscopic region where the relaxation takes place. The probability of a transition then becomes

$$\tau^{-1}(T) \propto P \propto \exp\left(\frac{-dV \sum_{ij} \sigma_{ij} \varepsilon_{ij} - T dS}{k_B T}\right) = \exp\left(\frac{dS}{k_B}\right) \cdot \exp\left(-C \frac{dV}{k_B T}\right) \quad (9)$$

One can assume that as the temperature is increased more internal states are accessible, leading to an accelerated rate of change in the respective internal crystalline volumes. An assumption of the form $\Delta V \propto T/(T_0 - T)$, leads to the modified VFT expression of equation 5. The interpretation here is that as the temperature T_0 is approached the mesoscopic volume tends towards infinity, meaning that constriction effects imposed by the boundary no longer play a significant role in the relaxation. Clearly, as T_0 is a singularity in the expression the behaviour is not valid in the immediate vicinity of T_0 . E_0 is the energy of the interface per unit surface area.

This model is further reinforced by the relaxation times of the second run, figure 8(b), where the VFT like process 2 is missing. The second measurement run was only made from 0 °C to 230 °C. The 1st process is still evident with approximately the same time scales as the 1st measurement run. It is largely stationary until the phase transition noted at approximately 100 °C, where it becomes Arrhenius. A further change is noted again at 170 °C (440 K) indicating a change in charge mobility along the grain boundaries. A summary of the fitting parameters is presented in table 3. In addition, two more Arrhenius processes are apparent in the fitting. The second process is replaced a regular Arrhenius relaxation, and an additional relaxation appears in the lower frequencies (noted as process 3 in figure 8(b)). The energies of activation are in the range reported by Markiewicz et al [16] for hopping processes between Fe^{3+} and Fe^{2+} traps induced by oxygen vacancies at grain boundaries and it is most likely the same in our case.

Process	Activation Energy [kJ/mol]	Prefactor [s]
Process 1	$360K < T < 420K$	28.7 ± 2.4
	$440K < T < 500K$	81.2 ± 4.5
Process 2	50.8 ± 3.6	2.64×10^{-14}
Process 3	90.1 ± 3.1	1.14×10^{-15}

Table 3: The fitting parameters for the Arrhenius processes of Figure 8(b)

5. Conclusions

BFO and its derivatives hold great promise for applications. However, they are not simple materials to produce because of the reactivity of Bismuth. Understanding the dielectric picture can help decipher an otherwise complicated mosaic. In this paper we have attempted to do just that using dielectric spectroscopy and the language of dielectric relaxation for a *BFO* ceramic tablet consisting of 70.5 % *BFO*, 27.7% $Bi_2Fe_4O_9$ and 1.8 % $Bi_{25}FeO_{40}$. The results reveal an unstable sample where the sintering process is still active. Grain boundary strains result if a partial onset of the Ferromagnetic phase transition at temperatures far lower than expected. A kinetic rearrangement of the sample is also revealed by the modification of the dc conductivity of the sample starting from 370 K. Furthermore, the non-Arrhenius relaxation in the first temperature run is explained by way of a thermodynamic model related to the coalition of differing sized crystalline particles. We feel that detailed dielectric studies of these ceramics and their derivatives can lead to more robust sintering regimes.

References

- [1] P. Curie, Sur la symétrie dans les phénomènes physiques, symétrie d'un champ électrique et d'un champ magnétique, *Journal de physique théorique et appliquée* 3 (1) (1894) 393–415.
- [2] G. Achenbach, W. James, R. Gerson, Preparation of single-phase polycrystalline $BiFeO_3$, *Journal of the American Ceramic Society* 50 (8) (1967) 437–437.
- [3] I. Velasco-Davalos, F. Ambriz-Vargas, G. Kolhatkar, R. Thomas, A. Ruediger, Synthesis of $BiFeO_3$ thin films on single-terminated $Nb : SrTiO_3$ (111) substrates by intermittent microwave assisted hydrothermal method, *AIP Advances* 6 (6) (2016) 065117.
- [4] G. Catalan, J. F. Scott, Physics and applications of bismuth ferrite, *Advanced materials* 21 (24) (2009) 2463–2485.
- [5] C. Michel, J.-M. Moreau, G. D. Achenbach, R. Gerson, W. J. James, The atomic structure of $BiFeO_3$, *Solid State Communications* 7 (9) (1969) 701–704.
- [6] D. V. Karpinsky, E. A. Eliseev, F. Xue, M. V. Silibin, A. Franz, M. D. Glinchuk, I. O. Troyanchuk, S. A. Gavrilov, V. Gopalan, L.-Q. Chen, et al., Thermodynamic potential and phase diagram for multiferroic bismuth ferrite (bifeo 3), *npj Computational Materials* 3 (1) (2017) 1–10.
- [7] A. Kadomtseva, Y. F. Popov, A. Pyatakov, G. Vorob'ev, A. Zvezdin, D. Viehland, Phase transitions in multiferroic $BiFeO_3$ crystals, thin-layers, and ceramics: enduring potential for a single phase, room-temperature magnetoelectric holy grail, *Phase Transitions* 79 (12) (2006) 1019–1042.

- [8] N. Wang, X. Luo, L. Han, Z. Zhang, R. Zhang, H. Olin, Y. Yang, Structure, performance, and application of $BiFeO_3$ nanomaterials, *Nano-Micro Letters* 12 (1) (2020) 1–23.
- [9] V. Shvartsman, W. Kleemann, R. Haumont, J. Kreisel, Large bulk polarization and regular domain structure in ceramic $BiFeO_3$, *Applied physics letters* 90 (17) (2007) 172115.
- [10] A. Crassous, R. Bernard, S. Fusil, K. Bouzehouane, D. Le Bourdais, S. Enouz-Vedrenne, J. Briatico, M. Bibes, A. Barthélémy, J. E. Villegas, Nanoscale electrostatic manipulation of magnetic flux quanta in ferroelectric/superconductor $BiFeO_3/YBa_2Cu_3O_7 - \delta$ heterostructures, *Physical review letters* 107 (24) (2011) 247002.
- [11] J. Allibe, S. Fusil, K. Bouzehouane, C. Daumont, D. Sando, E. Jacquet, C. Deranlot, M. Bibes, A. Barthelemy, Room temperature electrical manipulation of giant magnetoresistance in spin valves exchange-biased with $BiFeO_3$, *Nano letters* 12 (3) (2012) 1141–1145.
- [12] P. Hemme, P. Djemia, P. Rovillain, Y. Gallais, A. Sacuto, A. Forget, D. Colson, E. Charron, B. Perrin, L. Belliard, et al., Elastic properties assessment in the multiferroic $BiFeO_3$ by pump and probe method, *Applied Physics Letters* 118 (6) (2021) 062902.
- [13] A. Kirsch, M. M. Murshed, F. J. Litterst, T. M. Gesing, Structural, spectroscopic, and thermo-analytic studies on $Bi_2Fe_4O_9$: tunable properties driven by nano-and poly-crystalline states, *The Journal of Physical Chemistry C* 123 (5) (2019) 3161–3171.
- [14] K. J. MacKenzie, T. Dougherty, J. Barrel, The electronic properties of complex oxides of bismuth with the mullite structure, *Journal of the European Ceramic Society* 28 (2) (2008) 499–504.
- [15] M. Curti, T. M. Gesing, M. M. Murshed, T. Bredow, C. B. Mendive, Liebau density vector: a new approach to characterize lone electron pairs in mullite-type materials, *Zeitschrift für Kristallographie-Crystalline Materials* 228 (12) (2013) 629–634.
- [16] E. Markiewicz, B. Hilczer, M. Błaszyk, A. Pietraszko, E. Talik, Dielectric properties of $BiFeO_3$ ceramics obtained from mechanochemically synthesized nanopowders, *Journal of electroceramics* 27 (3-4) (2011) 154–161.
- [17] A. Perejón, E. Gil-González, P. E. Sánchez-Jiménez, A. R. West, L. A. Pérez-Maqueda, Electrical properties of bismuth ferrites: $Bi_2Fe_4O_9$ and $Bi_{25}FeO_{39}$, *Journal of the European Ceramic Society* 39 (2-3) (2019) 330–339.
- [18] G. Orr, A. Goryachev, G. Golan, Sintering bfo targets for rf sputtering, *BULGARIAN CHEMICAL COMMUNICATIONS* (2020) 40.
- [19] S. Chakraborty, M. Pal, Highly efficient novel carbon monoxide gas sensor based on bismuth ferrite nanoparticles for environmental monitoring, *New Journal of Chemistry* 42 (9) (2018) 7188–7196.
- [20] S. M. Selbach, M.-A. Einarsrud, T. Grande, On the thermodynamic stability of $BiFeO_3$, *Chemistry of Materials* 21 (1) (2009) 169–173.
- [21] J. Rodriguez-Carvajal, Fullprof: a program for rietveld refinement and pattern matching analysis, in: *satellite meeting on powder diffraction of the XV congress of the IUCr*, Vol. 127, Toulouse, France:[sn], 1990.

- [22] S. Gražulis, D. Chateigner, R. T. Downs, A. Yokochi, M. Quirós, L. Lutterotti, E. Manakova, J. Butkus, P. Moeck, A. Le Bail, Crystallography open database—an open-access collection of crystal structures, *Journal of applied crystallography* 42 (4) (2009) 726–729.
- [23] T. A. Para, S. K. Sarkar, Challenges in rietveld refinement and structure visualization in ceramics, in: *Advanced Ceramic Materials*, IntechOpen, 2021.
- [24] Alpha High Resolution dielectric Analyser (2000).
- [25] A. Patterson, The scherrer formula for x-ray particle size determination, *Physical review* 56 (10) (1939) 978.
- [26] M. E. Lines, A. M. Glass, Principles and applications of ferroelectrics and related materials, Oxford university press, 2001.
- [27] B. A. Strukov, A. P. Levanyuk, Ferroelectric phenomena in crystals: physical foundations, Springer Science & Business Media, 2012.
- [28] N. Krainik, N. Khuchua, V. Zhdanova, V. Esveev, Phase transitions in $BiFeO_3$, *Soviet Physics Solid State, USSR* 8 (3) (1966) 654–+.
- [29] M. A. Carpenter, E. K. Salje, A. Graeme-Barber, Spontaneous strain as a determinant of thermodynamic properties for phase transitions in minerals, *European Journal of Mineralogy* (1998) 621–691.
- [30] A. K. Jonscher, Universal relaxation law: a sequel to Dielectric relaxation in solids, Chelsea Dielectrics Press, 1996.
- [31] N. Axelrod, E. Axelrod, A. Gutina, A. Puzenko, P. B. Ishai, Y. Feldman, Dielectric spectroscopy data treatment: I. frequency domain, *Measurement Science and Technology* 15 (4) (2004) 755.
- [32] I. MathWorks, MATLAB: The Language of Technical Computing. Using MATLAB., Vol. 3, MathWorks, 2000.
- [33] A. Perejón, N. Masó, A. R. West, P. E. Sánchez-Jiménez, R. Poyato, J. M. Criado, L. A. Pérez-Maqueda, Electrical properties of stoichiometric $BiFeO_3$ prepared by mechanosynthesis with either conventional or spark plasma sintering, *Journal of the American Ceramic Society* 96 (4) (2013) 1220–1227.
- [34] F. Kremer, A. Schönhals, Broadband dielectric spectroscopy, Springer Science & Business Media, 2002.
- [35] F. Kremer, A. Schönhals, The scaling of the dynamics of glasses and supercooled liquids, in: *Broadband dielectric spectroscopy*, Springer, 2003, pp. 99–129.